Nano LiMnBO₃, a high-capacity cathode material for Li-ion batteries

Semih Afyon*, Dipan Kundu, Frank Krumeich, Reinhard Nesper

ETH Zurich, Department of Chemistry and Applied Biosciences, CH-8093 Zurich, Switzerland

HIGHLIGHTS

► Nano h-LiMnBO₃ was synthesized by a sol–gel method for the first time.
► A high first discharge capacity of 136 mAh g^{-1} was achieved for nano h-LiMnBO₃.
► Employing a composite electrode with RGO improved cycling stability.

ABSTRACT

Nano h-LiMnBO₃ with an average particle size of ∼20 nm has been synthesized by a sol–gel method for the first time. The nanoscopic material is obtained at temperatures of 350 °C and below, whereas the higher temperature synthesis above 500 °C results in the microcrystalline phases that have poorer electrochemical performance. In situ carbon coating of LiMnBO₃ particles by carbonization of propionic acid right during the synthesis of nano h-LiMnBO₃ (4.2 wt-% carbon) provides a conducting surface. Carbon particles partially cover the surfaces of nanorods and disperse among nano crystallites enhancing the electronic transport in the electrode material. The sol–gel synthesized nano h-LiMnBO₃ yields a first discharge capacity of 136 mAh g^{-1} within a window of 4.7–1.7 V at C/20 rate. This is considerably higher than previously reported. Further improvements of the system are realized by preparing a composite electrode of nano h-LiMnBO₃ with reduced graphite oxide that delivers a high first discharge capacity of 145 mAh g^{-1} at C/20 rate and retaining a discharge capacity of 111 mAh g^{-1} at the 10th cycle. An increase of capacity is expected to be reached by further reduction of the particle size and size spread as well as by optimizing the conductive coating of the nano particles.

1. Introduction

Since their commercialization in the 1990s, Li-ion batteries are widely used as the primary choice for secondary batteries due to their outstanding energy density. By having the advantages of high voltage, high capacity, long cycle life and variable charge–discharge rates, Li-ion batteries dominate the portable electronics market and most recently, plug-in electric vehicles powered by Li-ion batteries have entered into the market [1–3]. The conventional Li-ion batteries have LiMO₂ (M = Co, Ni, Mn) cathodes and graphite based anodes. However, the use of such oxides as cathode materials is a setback for the large scale use of plug-in

electric vehicles, when aspects like cost, energy density, and safety are considered. In order to address these problems, following the initial work of Goodenough et al. [4], olivine-type materials (LiMPO₄, M = Fe, Co, Ni, Mn) have been extensively investigated [5–16]. Although PO₄$^{3-}$ units are not electro-active, and thus detract from energy density, they introduce several advantages especially through a higher operating voltage due to the increased lattice potential, which also fixes oxygen atoms in the structure providing a chemical stability beyond LiMO₂ cathodes that act as strong oxidizing agents for organic electrolytes. For instance, LiFePO₄ operates at 3.5 V with a theoretical capacity of 170 mAh g^{-1} [17], and even though it suffers from poor ionic and electronic conductivity, the theoretical capacity is achievable for the material via nano-sizing and conductive (carbon) coatings [5,9,18,19]. In addition, iron and manganese-based olivines have considerable advantages in costs. At present, many companies have started to produce and commercialize LiFePO₄ and its composites that are currently one of the preferred choices as the cathode material for plug-in electric cars. However, all current

* Corresponding author. ETH Zurich, Laboratory of Inorganic Chemistry, Wolfgang Pauli Strasse 10, 8093 Zurich, Switzerland. Tel.: +41 44 633 4623; fax: +41 44 632 1149.

E-mail addresses: afyon@inorg.chem.ethz.ch (S. Afyon), kundu@inorg.chem.ethz.ch (D. Kundu), krumeich@inorg.chem.ethz.ch (F. Krumeich), reinhard.nesper@inorg.chem.ethz.ch (R. Nesper).

cathode materials are still not capable enough to satisfy the energy density demand required for the large scale use of electric vehicles. There is a need for cathode materials working at higher output voltages with higher practical capacities. Borates ($LiMBO_3$, M = Fe, Mn, Co) could be good alternatives to phosphates by having the lower weight BO_3^{3-} groups instead of PO_4^{3-}, but keeping the advantage of the linking anion group giving a higher operating voltage and enhanced structural stability. The idea was first introduced by Legagneur et al., but they were only able to extract 0.04 and 0.02 Li per formula unit for $LiFeBO_3$ and $LiMnBO_3$, respectively [20]. Recently, Yamada et al. achieved a high capacity of $\sim$190 mAh g^{-1} at C/20 rate for $LiFeBO_3$ by carbon composite formation and avoiding the exposure of the material to air [21]. There are two phases of $LiMnBO_3$ that has a theoretical capacity of $\sim$220 mAh g^{-1} [20,22]. For the monoclinic phase, the electrochemical activity has been shown by Kim et al.; the material synthesized by a conventional solid state method and further treated by ball-milling and carbon coating delivers a second discharge capacity of 100 mAh g^{-1} at C/20 [23]. For hexagonal-$LiMnBO_3$, most of the studies showed very low charge/discharge capacities so far [23–25]. Chen et al. claimed electrochemical activity for h-$LiMnBO_3$, but a charge/discharge capacity of only 75.5 mAh g^{-1} with a huge polarization at $\sim$C/40 rate was observed in the voltage window of 4.8–1.0 V [25]. The source of the capacity could be expected to be a conversion reaction rather than the lithiation/delithiation of h-$LiMnBO_3$ in the designated voltage range used in their study.

Similar to phosphates, lithium transition metal borates are considered to have intrinsically low ionic and electronic conductivity, which is believed to be the cause of the poor electrochemical performance of h-$LiMnBO_3$ so far [23,25]. Utilization of appropriate nano-particles can lead to diminish these effects and to aggravate charge/discharge capacities considerably. The use of nano-particles decreases the length of the diffusion paths for Li$^+$ ions and enhances electron hopping, thus, improving the electrochemical performance of the otherwise poorly conducting materials. Such materials have to be embedded in conductive matrices, which is generally done by conductive carbon coatings through various methods.

Here, we report the sol–gel synthesized nano h-$LiMnBO_3$ as a cathode material for Li-ion batteries for the first time. The material is obtained at a temperature as low as 350 °C and consists of nano crystallites with an average size of $\sim$20 nm. The composite electrode of nano h-$LiMnBO_3$ with reduced graphite oxide delivers a first discharge capacity of 145 mAh g^{-1} at C/20 rate, and it maintains a discharge capacity of 111 mAh g^{-1} at the 10th cycle. These are the best results reported so far for $LiMnBO_3$ to our knowledge.

2. Experimental section

2.1. Synthesis

Stable sols were obtained by dissolving stoichiometric amounts of $LiNO_3$, $MnNO_3 \cdot (H_2O)_4$ and $B(OEt)_3$ in propionic acid. In a typical synthesis, 0.01 mol $LiNO_3$ and 0.01 mol $MnNO_3 \cdot (H_2O)_4$ are dissolved in $\sim$10 ml propionic acid at 80 °C for 3 h, and similarly, 0.01 mol $B(OEt)_3$ in 30 ml propionic acid. After the salts are completely dissolved the two solutions are mixed and heated at 80 °C for an hour. 0.05 mol water are added for hydrolysis and a gel is obtained by evaporating the solvent at 80–100 °C. Annealing of the gel-powder at 350, 500, and 650 °C for 10 h under reductive CO atmosphere yields nano h-$LiMnBO_3$, crystalline h-$LiMnBO_3$ and crystalline m-$LiMnBO_3$ (or a mixture of crystalline phases), respectively.

Graphite oxide was synthesized from graphite by a modified Brodie method [27]. The composite material was obtained by ball-milling $\sim$66.6 wt-% nano h-$LiMnBO_3$ with $\sim$33.3 wt-% graphite oxide. To obtain reduced graphite oxide, the product was heated at 200–250 °C for 8 h under nitrogen atmosphere. Combustion-infrared spectroscopy analysis (LECO instruments, ETH LOC Micro-Laboratory) confirmed a final carbon content of $\sim$20 wt-% for the composite material.

2.2. Characterization

Powder X-ray diffraction patterns of the samples were recorded with a STOE Stadi P diffractometer equipped with a germanium monochromator and CuK$_{\alpha1}$ radiation (operated at 35 mA, 35 kV). The average crystallite sizes of samples were calculated by the Scherrer equation: Crystallite size $= 0.9\lambda/(\beta \cos \theta)$, where λ is the wavelength of incident X-rays, β is the full width at the half maximum of the (111) peak for h-$LiMnBO_3$, and θ is the Bragg angle.

Scanning electron microscopy (SEM) analysis was done with a Zeiss Gemini 1530 operated at 1 kV. Transmission electron microscopy (TEM) was carried out on a CM30ST (FEI; LaB$_6$ cathode) and a Tecnai F30 microscope (both operated at 300 kV and point resolution $\sim$2Å).

2.3. Electrochemical tests

For cathode fabrication, (70 wt-%) active material and (20 wt-%) conductive carbon (Super P® Timcal (or RGO) + in-situ carbon) were manually mixed and ball-milled for 1 h afterwards to ensure proper mixing. Then, 10 wt-% PVDF binder was mixed, and a slurry of the mixture in 1:4, toluene:THF solution was prepared by ultrasonic dispersion. The slurry was cast on Ti current collectors and dried at 80 °C under vacuum. The final electrodes consisted of approximately 2–3 mg active material. Li metal anodes were prepared from a 0.75 mm-thick ribbon (Aldrich), and 1 M solution of $Li[(C_2F_5)_3PF_3]$ in EC:DMC (1:1) (Merck, LF-30 SelectiLyte™) served as the electrolyte. Swagelok type of cells was constructed in an Ar filled glove-box. Galvanostatic tests were done in the voltage range of 4.7–1.7 V, and a potentiostatic step was applied at 4.7 V before discharging to 1.7 V. The cyclic voltammetry was carried out at a sweep rate of 0.05 mV s^{-1} within 4.7–1.7 V.

3. Results and discussion

Fig. 1 shows the crystal structures of the two modifications of $LiMnBO_3$. The reported structure [20] for the hexagonal phase (space group: P-6) (Fig. 1a) consists of MnO$_5$ square pyramids connected to each other via sharing of equatorial edges of the pyramids. Chains of MnO$_5$ polyhedra run along the c-axis and are connected to each other by planar BO$_3$ units. Li atoms are in tetrahedral coordination, and the LiO$_4$ tetrahedras form chains parallel to those of the square pyramids along the c-axis. In the monoclinic phase [22] (space group: C12/c1) (Fig. 1b), MnO$_5$ has a trigonal bipyramidal geometry, and similarly forms polyhedral chains by edge sharing along the [−101] direction. Trigonal planar BO$_3$ groups connect three polyhedra chains via corner sharing, and Li atoms are as well tetrahedrally coordinated by O atoms. According to the previous theoretical work, the preferred diffusion path of Li$^+$ ions in both phases has a one dimension character parallel to the c-axis [23].

Different crystalline materials of $LiMnBO_3$ and nano h-$LiMnBO_3$ have been synthesized by a sol gel method, where stable sols were obtained starting from stoichiometric amounts of $LiNO_3$, $MnNO_3 \cdot (H_2O)_4$ and $B(OEt)_3$ as precursors dissolved in propionic acid. By firing the gel-powder, obtained by evaporating the
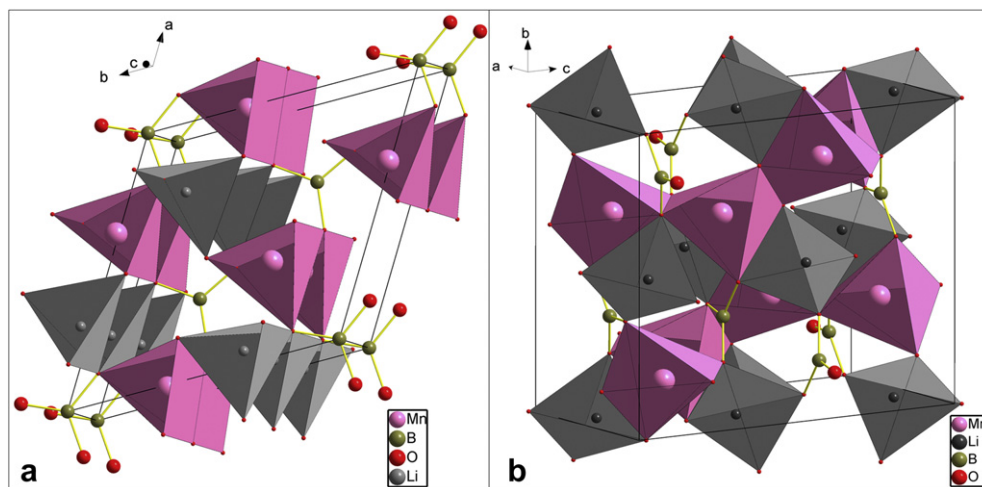
Fig. 1. Crystal structures of LiMnBO$_3$: a) skew [001] view of the hexagonal phase, b) skew [100] view of the monoclinic phase.

solution, under reductive CO atmosphere at 350, 500 and 650 °C, nano h-LiMnBO$_3$, crystalline h-LiMnBO$_3$ and crystalline m-LiMnBO$_3$ were produced, respectively. In situ carbon coating of LiMnBO$_3$ particles was also achieved by carbonization of propionic acid, though not in a homogeneous way as revealed by transmission electron microscopy images (TEM, Fig. 4). By combustion-infrared spectroscopy analysis, we found 4.2, 4.3 and 2.9 wt-% carbon in the samples of nano h-LiMnBO$_3$, crystalline h-LiMnBO$_3$ and crystalline m-LiMnBO$_3$ samples, respectively. XRD powder patterns of the sol–gel synthesized LiMnBO$_3$ materials and the theoretical diffraction patterns are displayed in Fig. 2. For both phases, all of the diffraction peaks can be matched to the theoretical patterns (ICSD 94318 and 200535), and residual diffraction peaks hinting impurities are not observed. In the XRD powder pattern of nano h-LiMnBO$_3$, some diffraction peaks (e.g. (111) reflection, $2\theta = 35.99$) are more intense due to disorder (Supplementary Fig. S1) and preferred orientation in nano crystallites. But, yet, most of the characteristic diffraction peaks of h-LiMnBO$_3$ are still present for the sample. In contrast to previous studies, where the hexagonal phase was obtained at a higher temperature than the monoclinic phase by solid state synthesis, we obtain nano h-LiMnBO$_3$ at a temperature as low as 350 °C. Annealing the gel-powder above 500 °C generates larger crystallites of h-LiMnBO$_3$, whereas the annealing above 600 °C leads either to pure m-LiMnBO$_3$ or to a mixture of h-LiMnBO$_3$ and m-LiMnBO$_3$. Even though our studies do not reveal much about the thermodynamic stability of the phases, the reductive atmosphere used during the synthesis and the exothermic combustion reaction could be speculated as the driving force for the formation of h-LiMnBO$_3$ at a low temperature. Nevertheless, the synthesis of nano h-LiMnBO$_3$ at 350 °C is reproducible, and pure m-LiMnBO$_3$ was also synthesized to compare the electrochemical performances of two phases.

Fig. 3 shows scanning electron microscopy (SEM) images of the sol–gel synthesized LiMnBO$_3$ powders. Nano h-LiMnBO$_3$ (Fig. 3a and b) consists of nanorods and smaller rounder particles, and has an average particle size of ~20 nm that is calculated by the broadening of (111) diffraction peak. As the annealing temperature increases, the particles coalesce and grow bigger, leading to an increase of the average crystallite size for h-LiMnBO$_3$ (Fig. 3c), at 500 °C to ~120 nm.

The SEM image of the monoclinic LiMnBO$_3$ is shown in Fig. 3d, and the shape of the particles is not very well defined. The crystallite size of m-LiMnBO$_3$ particles approximately ranges from 300 nm to 1 μ, but crystallites of 2–3 microns are also found.

Transmission electron microscopy images (TEM) and the electron diffraction (ED) pattern of nano h-LiMnBO$_3$ are presented in Fig. 4. The electron diffraction pattern (Fig. 4a) verifies the presence of nano h-LiMnBO$_3$ as the d-values calculated from the pattern
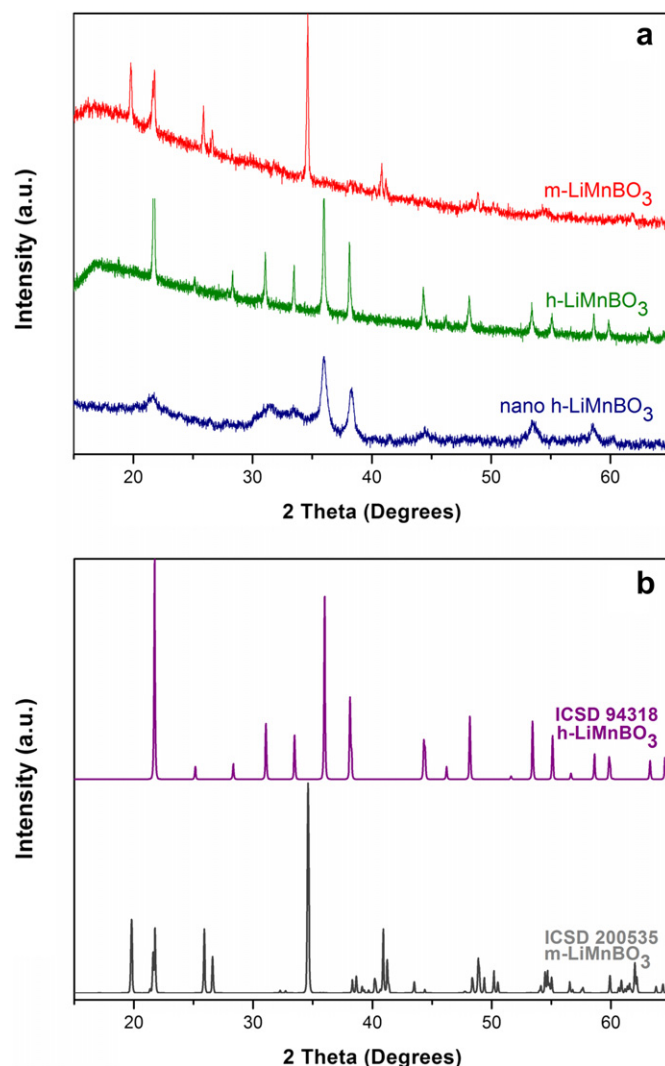

Fig. 2. XRD powder patterns of LiMnBO$_3$: a) experimental, b) calculated.
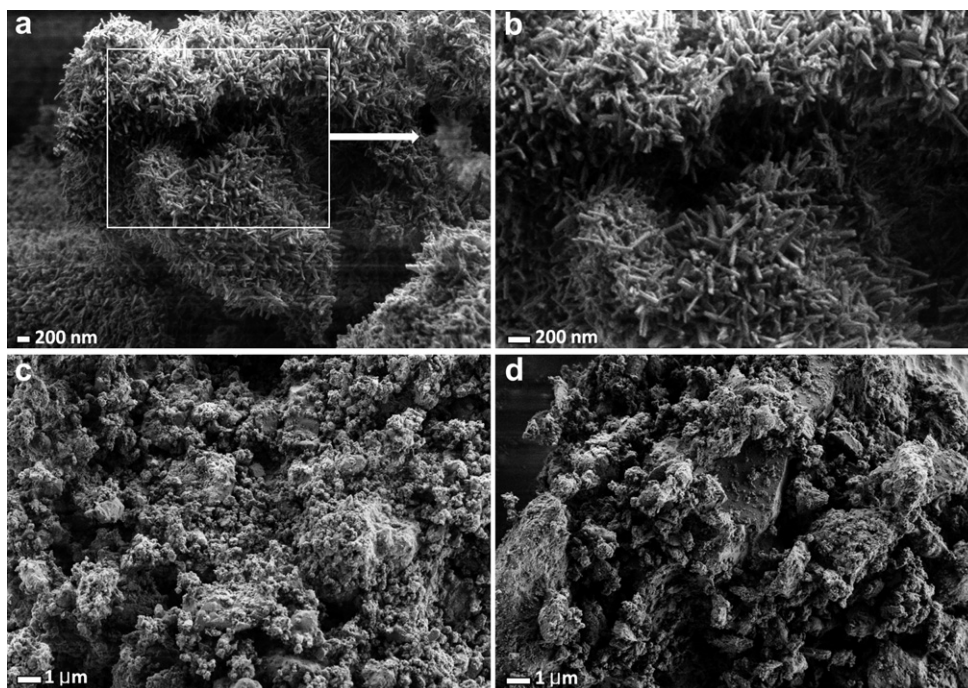
Fig. 3. Scanning electron microscopy (SEM) images of a) nano h-LiMnBO₃, b) zoomed in image of the marked region in (a) indicating nanorods, c) crystalline h-LiMnBO₃, d) crystalline m-LiMnBO₃.

correspond to the theoretical plane distances of hexagonal $LiMnBO_3$. Nanorods of h-$LiMnBO_3$ with dimensions ranging from 20 to 35 nm in width and 50–80 nm in length are displayed in Fig. 4b. The rounder particles of nano h-$LiMnBO_3$ that are smaller in size can also be seen in Fig. 4b, and more clearly in Fig. 4c, on the tip of a nanorod. As stated before, there are 4.2 wt-% carbon in nano h-$LiMnBO_3$ powder. The presence of the carbon coating on the rim of particles is evident from Fig. 4c. However, carbon particles do not cover the entire surfaces of the nano crystallites, but rather disperse among them, so that the conductive coating can still be enhanced. In addition, lattice fringes for the (110) planes of h-$LiMnBO_3$ are visible in high resolution images (Fig. 4c).

For the electrochemical characterization, electrodes consisting of approximately 2–3 mg active material on Ti current collectors were used as cathodes, and Li metal served as the anode. The working electrode was composed of (70 wt-%) active material, (20 wt-%) conductive carbon (Super P® + in-situ carbon) and (10 wt-%) PVDF binder. The electrolyte used for the electrochemical tests was 1 M solution of $Li[(C_2F_5)_3PF_3]$ in EC:DMC (1:1) (LF-30 SelectiLyte™). This electrolyte is considered to be electrochemically stable in the voltage window of our interest [26]. Consequently, we do not expect a major capacity contribution from the oxidation of the electrolyte in the high voltage limit. The galvanostatic charge/discharge curves for nano h-$LiMnBO_3$, crystalline h-$LiMnBO_3$ and crystalline m-$LiMnBO_3$ are presented in Fig. 5. The cells were cycled between 4.7 and 1.7 V by a combined galvanostatic–potentiosatic protocol. Galvanostatic (constant current) part was carried out at C/20 rate. Galvanostatic step in the charging process was followed by a potentiostatic step, where charging was carried out at the fixed upper voltage limit of 4.7 V, until the current dropped below 1 mA g^{-1}. The first discharge capacity of nano h-$LiMnBO_3$ (∼20 nm particles) is 136 mAh g^{-1}, and then drops to 118 mAh g^{-1} in the subsequent cycle. With increasing particle size, the hexagonal $LiMnBO_3$ (∼120 nm particles) only delivers a second discharge capacity of 49 mAh g^{-1}, and the value for the monoclinic $LiMnBO_3$ (sub-micron particles) remains at only 38 mAh g^{-1}. Clearly, this

finding shows that the particle size plays an important role for the electrochemical performance of $LiMnBO_3$ regardless of the phase in question. In the study of Kim et al., the second discharge capacity obtained for nano sized m-$LiMnBO_3$ (100 mAh g^{-1}) was higher than for micron sized h-$LiMnBO_3$ (10 mAh g^{-1}) In our study, nano h-$LiMnBO_3$ delivers the best specific capacity probably due to the reduced lengths of the diffusion paths for Li$^+$ ions and electrons.

The cyclic voltammetry study for nano h-$LiMnBO_3$ shows very broad oxidation and reduction peaks with apparent polarization (Fig. 6). The overpotential has been reduced after the first cycle that could be explained by the partial amorphization of nano h-$LiMnBO_3$. In the second cycle, the oxidation has an onset of ∼2.6 V, and the peak is at ∼4.1 V (close to the predicted average voltage in a previous study [23]), whereas the reduction peak is at ∼2.5 V, ranging from ∼4.0 to 1.9 V. The peak intensities have dropped at each cycle that is consistent with the capacity loss observed in galvanostatic measurements.

Despite in situ carbon coating, cycling stability remains problematic. The drastic drop in the second discharge capacity could be due to not fully reversible delithiation/lithiation stemming from partially hindered ionic and electronic conductivity. In order to counter this problem and further increase the charge/discharge capacity, we designed a composite electrode of nano h-$LiMnBO_3$ mixed with reduced graphite oxide (RGO). Graphite oxide was obtained from graphite by a modified Brodie method [27]. The composite electrode material was prepared by ball-milling nano h-$LiMnBO_3$ with graphite oxide and heating the product mixture at 200–250 °C for 8 h under nitrogen atmosphere to ensure reduction. After ball-milling and heat treatment, no residual diffraction peaks from graphite oxide could be observed in the XRD powder pattern of the composite (Supplementary Fig. S2) providing evidence for the reduction of graphite oxide to RGO, and the main diffraction peaks for nano h-$LiMnBO_3$ are not altered after the process showing that the phase was not decomposed or transformed. A TEM image of nano h-$LiMnBO_3$ coated with reduced graphite oxide (RGO) is shown in Fig. 7. The interlayer distance,
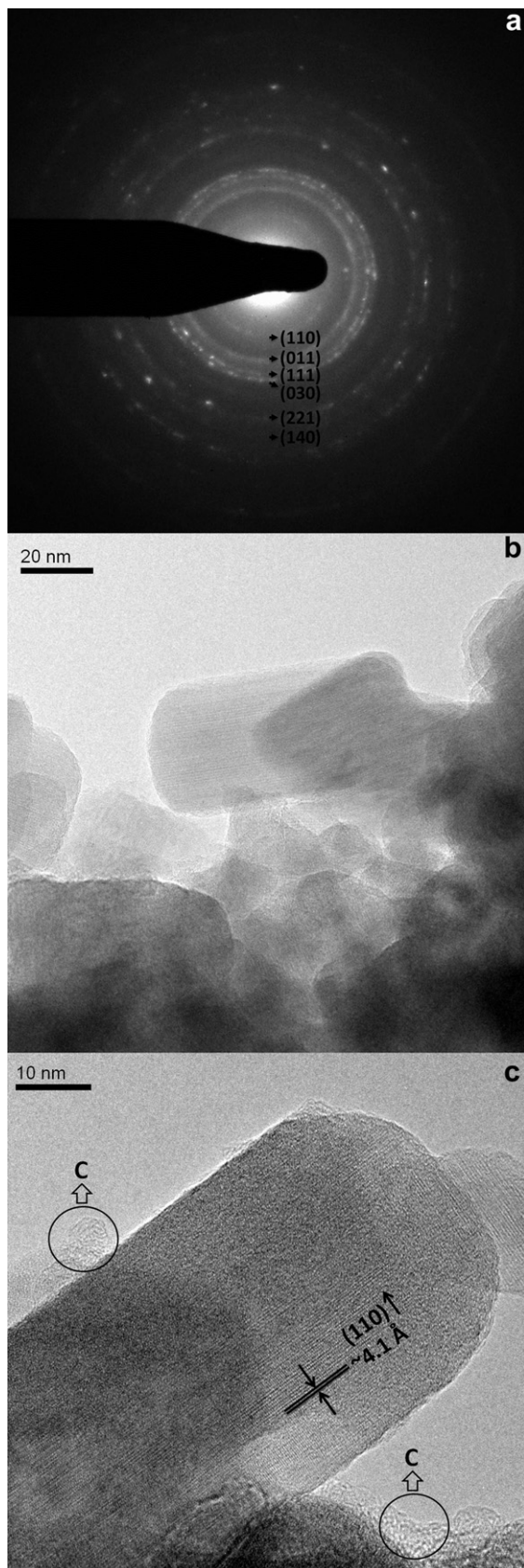
Fig. 5. Charge/discharge curves for LiMnBO$_3$ samples within 4.7–1.7 V at C/20 rate (constant voltage at 4.7 V until the current <1 mA g^{-1}): a) the first cycle of nano h-LiMnBO$_3$, b) the second cycle of nano h-LiMnBO$_3$, c) the second cycle of crystalline h-LiMnBO$_3$, d) the second cycle of crystalline m-LiMnBO$_3$.

~3.4 Å, of the coated material on nano h-LiMnBO$_3$ particles is close to the value for the (002) lattice spacing of graphite and indicates the presence of RGO on the surface. The TEM image also reveals that RGO does not only cover isolated particles, but rather forms a conductive network with embedded nano h-LiMnBO$_3$ particles. Fig. 8 shows the first five charge/discharge curves for the composite RGO/nano h-LiMnBO$_3$ electrode within a window of 4.7–1.7 V at C/20 rate. Similar to the prior carbon-coated nano h-LiMnBO$_3$ electrode, the composite electrode approximately contained 20 wt-% conductive carbon (RGO + in-situ carbon), and no additional conductive carbon source, besides the reduced graphite oxide and the carbon resulting from the synthesis, was used for the electrochemical tests. For the RGO/nano h-LiMnBO$_3$ composite, the first discharge capacity increases to 145 mAh g^{-1}, and there is reversible cycling at the 10th cycle with a discharge capacity of 111 mAh g^{-1}. Clearly, cycling properties as well as specific capacity are improved for the RGO/nano h-LiMnBO$_3$ composite compared to the prior described nano h-LiMnBO$_3$ electrode as illustrated in Fig. 9a. The average discharge capacity loss is approximately 2.3% per cycle for the RGO/nano h-LiMnBO$_3$ composite, whereas the value is 4.3% for the plain nano h-LiMnBO$_3$. The rate capability for the RGO/nano h-LiMnBO$_3$ is depicted in Fig. 9b. The discharge capacities in the range

Fig. 4. a) Electron diffraction (ED) pattern of nano h-LiMnBO$_3$ with identified diffraction rings, b) transmission electron microscopy image (TEM) of nano h-LiMnBO$_3$ showing nano crystallites, c) transmission electron microscopy (TEM) image of nano h-LiMnBO$_3$ showing the presence of in situ carbon particles and lattice fringes for the (110) planes of h-LiMnBO$_3$.
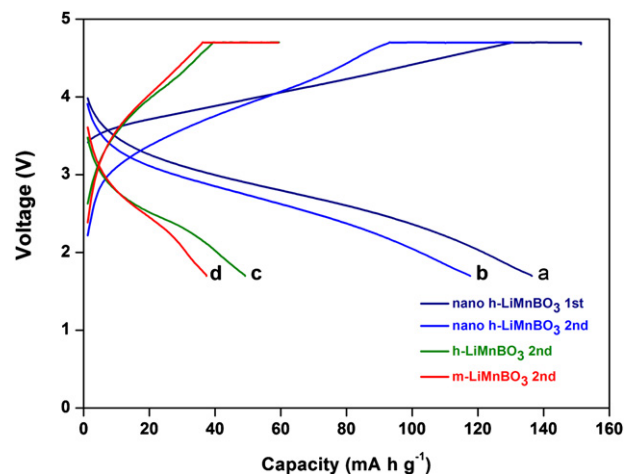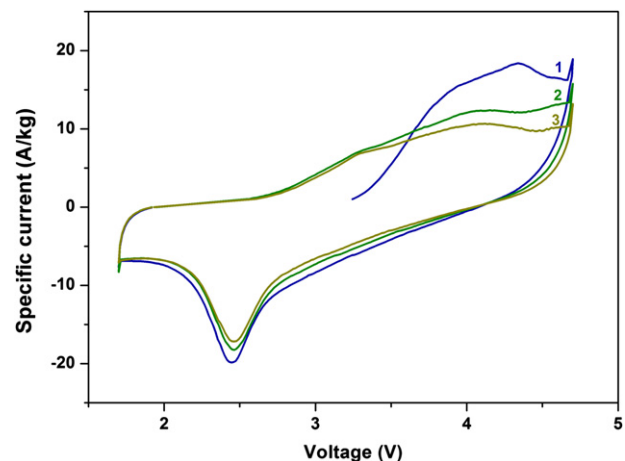

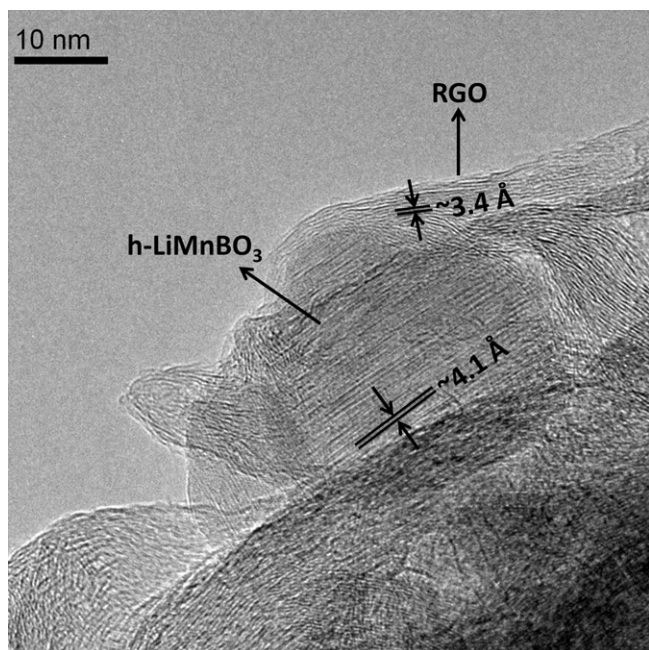**Fig. 6.** Cyclic voltammogram of nano h-LiMnBO$_3$ between 4.7 and 1.7 V at a scanning rate of 0.05 mV s^{-1}.

Fig. 7. Transmission electron microscopy (TEM) image of nano h-LiMnBO₃ coated by reduced graphite oxide (RGO).

of ~110, 102 and 77 mAh g^{-1} at the rates of C/10, C/5 and C/2 are obtained, respectively. The capacities decrease with increasing rate, but, yet, ~1/3 of the theoretical capacity is still delivered even at a rate of C/2. Considering the low ionic and electronic conducting nature of the material, this result is a significant improvement compared to the earlier work with various rates [25]. The enhanced properties for the RGO/nano h-LiMnBO₃ composite can be attributed to the covering and connecting of active nano h-LiMnBO₃ by RGO that is expected to facilitate electron and Li$^+$ ion transport. In addition, the RGO matrix may serve as a protective layer that can prevent the attack of by-products, such as HF, that might be formed during extensive cycling [28]. Furthermore, mechanical stability gained by the RGO network hinders capacity losses due to the pulverization and loss of interconnectivity during cycling.

XRD powder patterns of the electrodes of nano h-LiMnBO₃ in the charged and discharged states are depicted in Fig. 10. Even though it is hard to quantify the exact shift due to the broad diffraction peaks stemming from the nano nature of the compound,
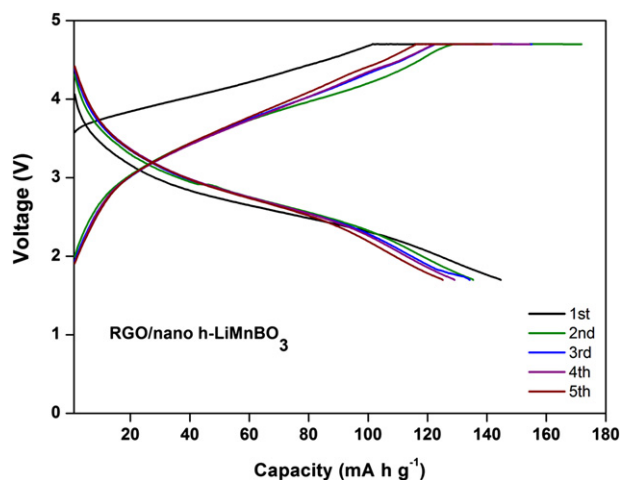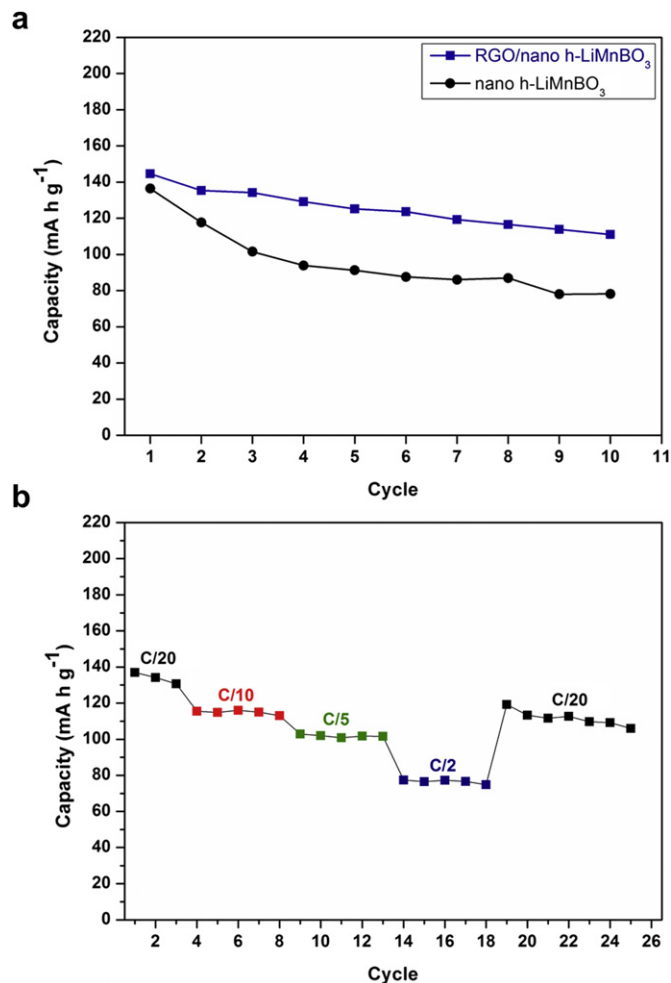

Fig. 9. a) Discharge capacity vs. cycle number for nano h-LiMnBO₃ (black) and RGO/nano h-LiMnBO₃ (blue), b) rate capability of RGO/nano h-LiMnBO₃. The cell was cycled within 4.7–1.7 V at C/20, C/10, C/5 and C/2 rates (at room temperature); before discharging, the voltage was retained constant at 4.7 V till the current dropped below C/100. (For interpretation of the references to colour in this figure legend, the reader is referred to the web version of this article.)
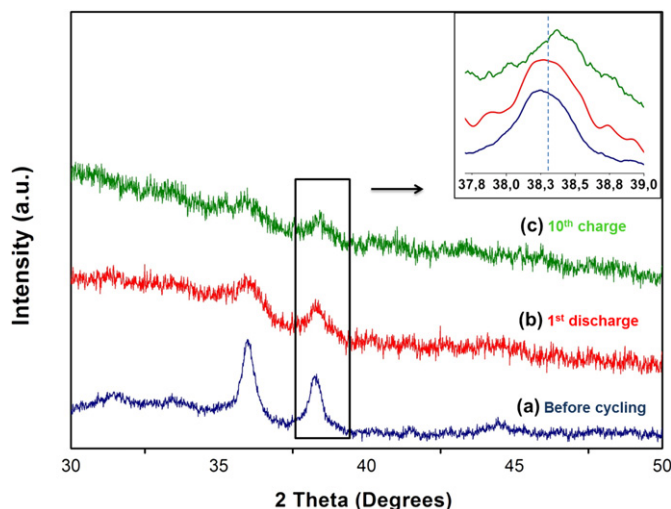

Fig. 8. Charge/discharge curves of RGO/nano h-LiMnBO₃ within 4.7–1.7 V at C/20 rate (constant voltage at 4.7 V until the current <1 mA g^{-1}) for the first five cycles.

Fig. 10. XRD powder patterns of the electrodes of nano h-LiMnBO₃ in the charged and discharged states: a) before cycling (blue), b) after first discharge to 1.7 V (red), c) after tenth charge to 4.7 V (green). (For interpretation of the references to colour in this figure legend, the reader is referred to the web version of this article.)
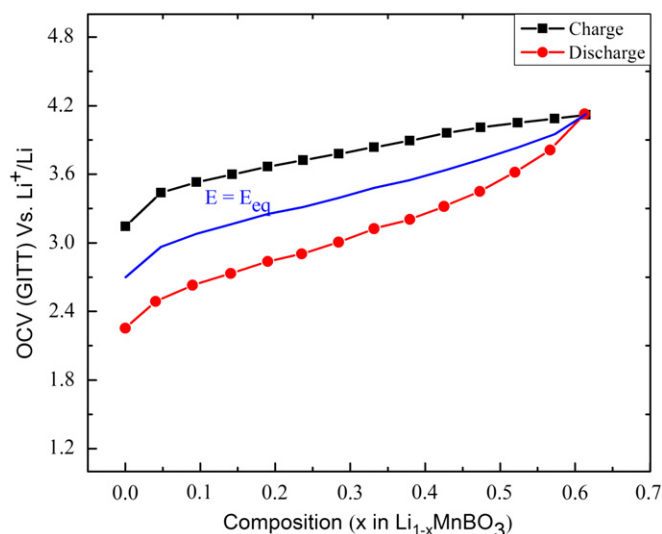
Fig. 11. OCV (open circuit voltage, the steady state voltage at the end of each open circuit step in GITT measurement, during charge (black), during discharge (red), average (blue)) vs. composition (x in $Li_{1-x}MnBO_3$). (For interpretation of the references to colour in this figure legend, the reader is referred to the web version of this article.)

it can be seen that the major diffraction peaks slightly shift between charged and discharged states. As suggested by the broadening of diffraction peaks, particles become smaller on cycling. The sloping character of charge/discharge curves of nano h-LiMnBO$_3$ and the diffraction peak shifts without occurrence of new phases provide evidence for a solid solution lithiation/delithiation mechanism. Galvanostatic Intermittent Titration Technique (GITT) was applied as well to determine the thermodynamic voltage composition relation. Fig. 11 represents the relation of OCV (open circuit voltage) with composition (x in $Li_{1-x}MnBO_3$), obtained by plotting the steady state voltage at the end of each open circuit step. The sloping nature of the OCV profile further supports that the Li^+ extraction/insertion proceeds as a single phase reaction. This also allows the application of GITT for the determination of lithium diffusion coefficients; the detailed results and experimental information on GITT are given in Supplementary data.

Ongoing amorphization of LiMnBO$_3$ upon cycling may be one of the reasons for the capacity loss. The RGO coating and linkage of the particles decrease this problem by keeping the connectivity much better. However, even for the RGO coated samples, capacity fading is still noticeable that could be caused by several factors: Mn dissolution into the electrolyte might be one, as observed for cycling of Mn-oxides [29,30] and LiMnPO$_4$ [31]; parts of the nanorods (35 × 80 nm, W × L) in our samples could still be too large for a fully reversible delithiation/lithiation considering the low ionic and electronic conductivity of the material; finally, unexpected SEI formation may increasingly separate active particles from the RGO network.

We expect a performance close to the theoretical capacity and better cycling by utilizing even smaller particles of h-LiMnBO$_3$ combined with a more sophisticated coating and network formation process.

4. Conclusion

Hexagonal and monoclinic phases of LiMnBO$_3$ were synthesized by a sol–gel method. In situ carbon coating of LiMnBO$_3$ particles by carbonization of propionic acid was realized during the synthesis, leading to partially carbon covered active particles. Nano h-LiMnBO$_3$ with an average particle size of ∼20 nm delivered a relatively high first discharge capacity of 136 mAh g^{-1} within 4.7–1.7 V at C/20 rate.

The improved performance compared to older investigations is attributed to the small particle size and in situ carbon coating. Further improvement of capacity and cycling properties were achieved by employing a composite electrode of active material and reduced graphite oxide. The first discharge capacity increased to 145 mAh g^{-1} for the RGO/nano h-LiMnBO$_3$ composite, and most of the capacity was retained over multiple cycles. The enhanced properties were ascribed to the RGO matrix facilitating electron transport and acting as a protective layer. The advances made on LiMnBO$_3$ are encouraging not only for the use of borate based compounds but also other materials of low kinetics for use as high energy cathodes for Li-ion batteries. Further studies are still necessary to enhance cycling performance and reduce kinetic polarization. To our knowledge, these are the best results reported so far for LiMnBO$_3$ opening more room for improvement of the electrochemical performance of kinetically hindered electrode materials.

Appendix A. Supplementary data

Supplementary data related to this article can be found at http://dx.doi.org/10.1016/j.jpowsour.2012.09.099.

References

[1] Mitsubishi-motors, Mitsubishi Innovative Electric Vehicle (May 2012). http://www.mitsubishi-motors.com/special/ev/.
[2] Nissan, Nissan Leaf Electric Car (May 2012). http://www.nissan-global.com/EN/NISSAN/LEAF/.
[3] Tesla-Motors, Tesla Roadster Electric Car (May 2012). http://www.teslamotors.com/goelectric.
[4] A.K. Padhi, K.S. Nanjundaswamy, J.B. Goodenough, J. Electrochem. Soc. 144 (1997) 1188–1194.
[5] K.F. Hsu, S.Y. Tsay, B.J. Hwang, J. Mater. Chem. 14 (2004) 2690–2695.
[6] H.M. Xie, R.S. Wang, J.R. Ying, L.Y. Zhang, A.F. Jalbout, H.Y. Yu, G.L. Yang, X.M. Pan, Z.M. Su, Adv. Mater. 18 (2006) 2609–2613.
[7] Y.H. Gu, C.S. Zeng, H.K. Wu, H.Z. Cui, X.W. Huang, X.B. Liu, C.L. Wang, Z.N. Yang, H. Liu, Mater. Lett. 61 (2007) 4700–4702.
[8] Y.S. Hu, Y.G. Guo, R. Dominko, M. Gaberscek, J. Jamnik, J. Maier, Adv. Mater. 19 (2007) 1963–1966.
[9] S.Y. Lim, C.S. Yoon, J.P. Cho, Chem. Mater. 20 (2008) 4560–4564.
[10] F. Wu, G.Q. Tan, R.J. Chen, L. Li, J. Xiang, Y.L. Zheng, Adv. Mater. 23 (2011) 5081–5085.
[11] J. Wolfenstine, J. Allen, J. Power Sources 136 (2004) 150–153.
[12] L.Y. Xing, M. Hu, Q. Tang, J.P. Wei, X. Qin, Z. Zhou, Electrochim. Acta 59 (2012) 172–178.
[13] G.H. Li, H. Azuma, M. Tohda, Electrochem. Solid State 5 (2002) A135–A137.
[14] F. Zhou, K.S. Kang, T. Maxisch, G. Ceder, D. Morgan, Solid State Commun. 132 (2004) 181–186.
[15] D. Choi, D. Wang, I.-T. Bae, J. Xiao, Z. Nie, W. Wang, V.V. Viswanathan, Y.J. Lee, J.-G. Zhang, G.L. Graff, Z. Yang, J. Liu, Nano Lett. 10 (2010) 2799–2805.
[16] H.S. Fang, L.P. Li, G.S. Li, Chem. Lett. 36 (2007) 436–437.
[17] H. Matsui, T. Nakamura, Y. Kobayashi, M. Tabuchi, Y. Yamada, J. Power Sources 195 (2010) 6879–6883.
[18] M.M. Doeff, J.D. Wilcox, R. Kostecki, G. Lau, J. Power Sources 163 (2006) 180–184.
[19] H.B. Gul, D.K. Jun, G.C. Park, B. Jin, E.M. Jin, J. Nanosci. Nanotechnol. 7 (2007) 3980–3984.
[20] V. Legagneur, Y. An, A. Mosbah, R. Portal, A.L. La Salle, A. Verbaere, D. Guyomard, Y. Piffard, Solid State Ionics 139 (2001) 37–46.
[21] A. Yamada, N. Iwane, Y. Harada, S. Nishimura, Y. Koyama, I. Tanaka, Adv. Mater. 22 (2010) 3583–3587.
[22] O.S. Bondareva, M.A. Simonov, Y.K.E. Tismenko, N.V. Belov, Kristallografiya 23 (1978) 487–490.
[23] J.C. Kim, C.J. Moore, B. Kang, G. Hautier, A. Jain, G. Ceder, J. Electrochem. Soc. 158 (2011) A309–A315.
[24] J.L. Allen, K. Xu, S.S. Zhang, T.R. Jow, Mater. Res. Soc. Symp. P. 730 (2002) 9–14.
[25] L. Chen, Y. Zhao, X. An, J. Liu, Y. Dong, Y. Chen, Q. Kuang, J. Alloy Compd. 494 (2010) 415–419.
[26] M. Schmidt, U. Heider, A. Kuehner, R. Oesten, M. Jungnitz, N. Ignat'ev, P. Sartori, J. Power Sources 97–98 (2001) 557–560.
[27] H.P. Boehm, A. Clauss, U. Hofmann, G.O. Fischer, Z. Naturforsch. Part B B 17 (1962) 150–153.
[28] K.-S. Lee, S.-T. Myung, K. Amine, H. Yashiro, Y.-K. Sun, J. Mater. Chem. 19 (2009) 1995–2005.
[29] S. Komaba, N. Kumagai, T. Sasaki, Y. Miki, Electrochemistry 69 (2001) 784–787.
[30] J.S. Chen, L.F. Wang, B.J. Fang, S.Y. Lee, R.Z. Guo, J. Power Sources 157 (2006) 515–521.
[31] S.-M. Oh, S.-W. Oh, C.-S. Yoon, B. Scrosati, K. Amine, Y.-K. Sun, Adv. Funct. Mater. 20 (2010) 3260–3265.